

Estimation of Parameters of Gravitational Wave Signals from Coalescing Binaries.

R. Balasubramanian and S. V. Dhurandhar

Inter-University Centre for Astronomy and Astrophysics,

Post Bag 4, Ganeshkhind, Pune 411 007, India.

(August 21, 2019)

Abstract

With the on going construction of several large and medium scale laser interferometric gravitational wave antennas around the globe, the problem of the detection of gravitational waves has acquired great impetus. Since gravitational wave signals from astrophysical sources are expected to be weak, despite the state of the art technology being employed, the development of optimal signal extraction techniques and the consequent accurate determination of the parameters of the signal is of major importance. Coalescing binary systems are one of the most promising sources of gravitational waves. One reason is that such sources are easier to model and thus one can design detection strategies tuned to such signals. A lot of attention has been devoted in the literature studying such techniques and most of the work has revolved around matched filtering and maximum likelihood estimation.

In a previous work, Monte Carlo simulations were carried out of the detection process using matched filtering for the initial LIGO/VIRGO configuration for the first post-Newtonian corrected coalescing binary waveform. We had compared the results of our simulations with available estimates, obtained from covariance matrix considerations, of the errors in the determination of the parameters. Our results showed that the covariance matrix

underestimates, by over a factor of two, the actual errors in the estimation of parameters even when the signal-to-noise ratio (SNR) is as high as 10. Sources having SNR higher than 10 are expected to be few and hence this issue is of major concern.

In this paper we probe the question as to why the Monte Carlo simulations give such high errors as opposed to those obtained via the covariance matrix. We present, a *computationally viable* statistical model of the distribution, of the maximum likelihood estimates (MLE), of the parameters. This model reproduces the essential features of the Monte Carlo simulations, thereby explaining the large root mean square errors in the estimates, obtained in numerical experiments. The chief reason for the large errors seems to be the fact that the probability distribution of the estimated parameters is multimodal. Though only the central peak (corresponding to the actual values of the parameters) is dominant, the subsidiary peaks occur ‘far’ away thereby contributing to large variances. We suggest that the variance or the standard deviation of an estimated parameter may not provide the best measure of the error, for the kind of situation we encounter here. We therefore propose another criterion by which the MLE should be judged.

In order to illustrate the model we have considered the Newtonian as well as the first post-Newtonian corrected waveform. We have assumed Gaussian noise, with a power spectrum typical of the LIGO/VIRGO type of detectors. The model we have used, however, is quite general, and robust, and will be relevant to many other parameter estimation problems.

PACS numbers: 04.30.+x, 04.80.+z

I. INTRODUCTION

Large scale laser interferometric detectors of gravitational waves, namely, the LIGO [1] and VIRGO [2] and the medium scale detectors, GEO and TAMA are expected to be operational by the turn of this century. Compact coalescing binary systems of blackholes and/or neutron stars are relatively ‘clean’ systems to model during their inspiral and their inspiral waveform can be predicted with a fair degree of reliability. This makes them the most promising sources for broad band detectors, and in particular, the upcoming interferometric detectors cited above. Binary systems are also valuable sources of astrophysical information as one can probe the universe up to cosmological distances. For instance, statistical analysis of several binary coalescences enables the estimation of the Hubble constant to an accuracy better than 10% [3–5]. Events that produce high signal-to-noise ratio can be potentially used to observe such non-linear effects, as gravitational wave tails, and to put general relativity into test in the strongly non-linear regime [6]. Due to the weak coupling of gravitational radiation with matter the signal waveform has a very low amplitude and will not stand above the detector noise. In addition to the on-going efforts to reduce the noise, and hence increase the sensitivity of the detector, a considerable amount of research activity has gone into the development of efficient and robust data analysis techniques to extract signals buried in very noisy data. For a review on gravitational waves from compact objects and their detection see Thorne [7,8].

Various data analysis schemes have been proposed for the detection of the ‘chirp’ waveform from such systems. Among them the technique of matched filtering is the most promising [9–11]. Briefly, this technique involves correlating the detector output with a set of templates, each of which is tuned to detect the signal with a particular set of parameters. In order to obtain a high value for the correlation the signal waveform should be known to a high level of accuracy. The matched filtering technique is very sensitive to the *phase* of the signal and even if the template and the signal mismatch by even half a cycle the correlation integral is drastically reduced.

The fully general relativistic waveform from a coalescing binary system of stars is as yet unavailable. In the absence of such an exact solution, there have been efforts to find solutions perturbatively. Most of the work in this area strives towards computing the waveform correct to a high degree of accuracy so that the theoretical templates based on this will obtain the maximum possible SNR.

The signal is said to be detected, if the maximum value of the correlation over all the parameters of the signal crosses a preassigned threshold which has been set by the false alarm one is prepared to tolerate. Once the signal is detected, the maximum likelihood estimates (MLE) of the parameters of the binary are those of the template with which the maximum correlation is obtained. The errors involved in such an estimation have been worked out by several authors [6,12–18], for the case of ‘high’ SNR and for the Newtonian and post-Newtonian waveforms using a single and a network of detectors. In [19] exhaustive Monte Carlo numerical simulations were carried out to compute the errors in the estimation of parameters and covariances among them, for the case of the initial LIGO configuration taking into account only the first post-Newtonian corrections and assuming circular orbits. It was found that the errors as obtained from the simulations were larger by a factor of two or more from the errors as computed via the covariance matrix at astrophysically relevant SNRs. The discrepancy disappears as the SNR increases beyond certain value - typically 15 in the Newtonian case and 25 in the post-Newtonian case. The comparison with other less stringent lower bounds has also not resolved the discrepancy. Nicholson and Vecchio [20] have recently computed Bayesian bounds such as the Weiss-Wainstein and Ziv-Zakai, for the case of Newtonian signals. They conclude that though these bounds are tighter than the Cramer-Rao bound, the numerical errors are still much larger than the computed lower bounds.

In this paper we explain the discrepancy between the Monte Carlo simulations and the results obtained from the covariance matrix. We demonstrate that the probability distribution of the estimated parameters cannot be got from ‘local’ methods such as the ones used earlier [12]. Since our main purpose in this paper is to demonstrate the validity of

the statistical model, we initially use the simplified Newtonian model of the waveform. In the Newtonian case there are fewer parameters of the signal that one has to deal with, making the investigations simpler, analytically as well as computationally. We then specialize to the first post-Newtonian case. Here, although the discrepancy is larger, the problem is similar at a qualitative level.

Following Finn [12] we obtain an equation which relates the estimated parameters to the actual parameters of the signal for a given noise realisation. This equation is non-linear. Finn linearises the equation and obtains the errors in terms of the covariance matrix. Here we do not linearise the equation. We find that the equation has multiple solutions for the parameters in a certain sense and it is this multiplicity of roots forming islands in the parameter space which contributes significantly to the errors. Thus the problem is of a global nature and any local approximation will be inadequate in explaining away the errors. Moreover we suggest that the variance/covariance of the parameters is not a proper measure of the errors in this case. We therefore propose a new criterion by which the MLE should be judged.

The paper is organized as follows. In section II we briefly describe the gravitational wave signal waveform and the parameters on which it depends, namely, the amplitude, the time of arrival, the phase at arrival and the ‘chirp times’, which characterizes the time for the binary to evolve from some fiducial time to the actual merger. These parameters are found to be very convenient when we carry out Monte Carlo simulations. It turns out that the covariance matrix is independent of these parameters and hence it is sufficient to carry out the simulations only for a particular set of parameters. Further in this section we also describe the characteristics of the noise that we assume will be present in the detector and briefly review the matched filtering technique. In section III we present the results of the Monte Carlo simulations for the Newtonian case. We carry out transformations of the parameter space which bring out the chief features of the distribution of the estimated parameters. We show that the estimated parameters do not lie in a simply connected region around the signal parameters, but instead are distributed in multiple ‘islands’ in the

parameter space considered. We next present a geometric representation of our statistical model. We then apply this model to the Newtonian chirp waveform, and compare the model with the Monte Carlo simulations. In section IV we deal with the post-Newtonian waveform. Finally in section V we summarise our results. We propose an alternative measure for the error which performs reasonably better than the variance as a measure of the error.

II. THE SIGNAL AND THE NOISE

A. The Chirp Signal

When constructing templates for on-line detection, it is sufficient to work with the so called *restricted* post-Newtonian gravitational waveform. In this approximation the post-Newtonian corrections are incorporated only in the phase of the waveform, while ignoring corresponding corrections to the amplitude [21]. Consequently, the restricted post-Newtonian waveforms only contain the dominant frequency equal to twice the orbital frequency of the binary computed up to the relevant order. In the restricted post-Newtonian approximation the gravitational waves from a binary system of stars, modeled as point masses orbiting about each other in a circular orbit, induce a strain $s(t)$ at the detector given by

$$s(t) = \mathcal{A}(\pi f(t))^{2/3} \cos [\varphi(t) + \Phi], \quad (2.1)$$

where $f(t)$ is the instantaneous gravitational wave frequency, the constant \mathcal{A} involves the distance to the binary, its reduced and total mass, and the antenna pattern of the detector [9] and Φ is the initial phase of the wave at some fiducial time $t = t_s$. The phase of the waveform $\varphi(t)$ contains several pieces corresponding to different post-Newtonian contributions which can be schematically written as

$$\varphi(t) = \varphi_0(t) + \varphi_1(t) + \varphi_{1.5}(t) + \dots \quad (2.2)$$

The evolution of the phase depends on the masses of the two components of the binary, characterised by the reduced mass, μ and the total mass, M of the system. Here $\varphi_0(t)$ is the

dominant Newtonian part of the phase and $\varphi_n(t)$ represents the n th order post-Newtonian correction to it. The Newtonian part of the phase is sensitive only to a particular combination of the masses of the two stars, frequently characterised by its ‘chirp mass’, $\mathcal{M} = \mu^{3/5} M^{2/5}$.

We give below the waveform correct to the first post-Newtonian order:

$$\begin{aligned}\varphi_0(t) &= \frac{16\pi f_s \tau_0}{5} \left[1 - \left(\frac{f}{f_s} \right)^{-5/3} \right], \\ \varphi_1(t) &= 4\pi f_s \tau_1 \left[1 - \left(\frac{f}{f_s} \right)^{-1} \right]\end{aligned}\tag{2.3}$$

where $f(t)$ is given implicitly by,

$$t - t_s = \tau_0 \left[1 - \left(\frac{f}{f_s} \right)^{-8/3} \right] + \tau_1 \left[1 - \left(\frac{f}{f_s} \right)^{-2} \right],\tag{2.4}$$

where τ_0 and τ_1 are constants having dimensions of time given by

$$\begin{aligned}\tau_0 &= \frac{5}{256} \mathcal{M}^{-5/3} (\pi f_s)^{-8/3}, \\ \tau_1 &= \frac{5}{192\mu(\pi f_s)^2} \left(\frac{743}{336} + \frac{11}{4}\eta \right),\end{aligned}\tag{2.5}$$

where $\eta = \mu/M$, and f_s is the instantaneous gravitational wave frequency of the signal at $t = t_s$. The time elapsed starting from an epoch when the gravitational wave frequency is f_s till the epoch when it becomes infinite will be referred to as the *chirp time* of the signal. In the quadrupole approximation τ_0 is the chirp time whereas it is $\tau_0 + \tau_1$ for the first post-Newtonian case [22]. The Newtonian part of the phase is characterised by three parameters: (i) the *time of arrival* t_s when the signal first becomes *visible* in the detector, (ii) the *phase* Φ of the signal at the time of arrival and (iii) the chirp mass. At this level of approximation two coalescing binary signals of the same chirp mass but of different sets of individual masses would be degenerate and thus exhibit exactly the same time evolution. This degeneracy is removed when post-Newtonian corrections are included. The parameters t_s and Φ are *kinematical* that fix the origin of the measurement of time and phase, respectively, while the Newtonian and the post-Newtonian chirp times are *dynamical* parameters in the sense that they dictate the evolution of the phase and the amplitude of the signal.

The parameters τ_0 , τ_1 and t_s have the dimensions of time. We convert them to dimensionless parameters by multiplying them with $2\pi f_s$. Thus we have the parameter set,

$$\boldsymbol{\mu} \equiv \{\mu^0, \mu^1, \mu^2, \mu^3, \mu^4\} \equiv \{A, 2\pi f_s t_s, \Phi, 2\pi f_s \tau_0, 2\pi f_s \tau_1\}.$$

In the stationary phase approximation the Fourier transform of the restricted second-post-Newtonian chirp waveform for positive frequencies is given by [9,23,13,16].

$$\tilde{s}(f) = A\mathcal{N}f^{-7/6} \exp \left[i \sum_{j=1}^4 \chi_j(f) \mu^j - i \frac{\pi}{4} \right], \quad (2.6)$$

where A , is the amplitude parameter depending on the distance to the binary, as well as the chirp mass and \mathcal{N} is a normalization constant to be fixed by means of a scalar product to be introduced later, and

$$\begin{aligned} \chi_1 &= \frac{f}{f_s}, \\ \chi_2 &= -1, \\ \chi_3 &= \frac{f}{f_s} - \frac{8}{5} + \frac{3}{5} \left(\frac{f}{f_s} \right)^{-5/3}, \\ \chi_4 &= \frac{f}{f_s} - 2 + \frac{f_s}{f}. \end{aligned} \quad (2.7)$$

For $f < 0$ the Fourier transform is computed using the identity $\tilde{s}(-f) = \tilde{s}^*(f)$ obeyed by real functions $s(t)$.

B. The noise

The output of a gravitational wave detector such as the LIGO, will comprise of data segments, each of duration T seconds, uniformly sampled with a sampling interval of Δ , giving the number of samples in a single data train to be $N = T/\Delta$. Each data train can be considered as a N -tuple $\mathbf{x} \equiv \{x^0, x^1, \dots, x^{N-1}\}$, x^a being the value of the output of the detector at time $a\Delta$. The set of all such N -tuples constitutes an N -dimensional vector space \mathcal{V} where the addition of two vectors is accomplished by the addition of corresponding time samples. For later convenience we allow each sample to take complex values. A natural basis

for this vector space is the *time basis* $\mathbf{e}_r^a = \delta_r^a$ where r and a are the vector and component indices respectively. Another basis which we shall use extensively is the Fourier basis.

A gravitational wave signal from a coalescing binary system can be characterised by a set of parameters $\mu^a, a = 0, 1, \dots, m - 1$ belonging to some open set of the m -dimensional real space R^m . The set of such signals $\mathbf{s}(t; \boldsymbol{\mu})$ constitutes a m -dimensional manifold \mathcal{S} which is embedded in the vector space \mathcal{V} . Note that Greek characters in boldface denote the full collection of parameters characterising the signal. The parameters of the binary can be regarded as coordinates on the manifold. The basic problem of signal analysis is thus to determine whether the detector output vector \mathbf{x} is the sum of a signal vector and a noise vector, $\mathbf{x} = \mathbf{s} + \mathbf{n}$, or just the noise vector, $\mathbf{x} = \mathbf{n}$, and furthermore to identify which particular signal vector, among all possible. The latter is relevant to this paper where we are interested in estimating the parameters and also the errors made in such a estimation. Errors in the estimation arise because the noise contaminates the data.

The noise in ground based laser interferometric detectors will have, in general, both a Gaussian and a non-Gaussian component. The main sources for the Gaussian component are the shot noise due to photon counting, the thermal noise in the mirror suspensions along with the mirror itself and seismic noise. The non-Gaussian component can be contributed by numerous sources like sudden strain releases in the mirror suspension wires or even if lightning strikes. It should be possible to remove most of the non-Gaussian component by using environmental monitors and looking for coincidence among detectors located at widely separated sites. It is, therefore, assumed usually that the detector noise will be a Gaussian random process. Over a time scale of hours, it can also be assumed to be stationary.

The power spectral density of the Gaussian noise component rises very steeply towards the low frequency end due to seismic effects. At the high frequency end it is dominated by photon shot noise which leads to a rise towards higher frequencies. Thus the data will have to be bandpassed with a low frequency seismic cutoff, f_s , and a high frequency cutoff, f_c . We use the power spectral density expected for the initial LIGO as given in [1]. Accordingly, we choose $f_s = 40$ Hz and $f_c = 800$ Hz.

In the absence of the signal the output will contain only noise drawn from a stochastic process which can be described by a probability distribution on the vector space \mathcal{V} . We assume that the noise has its mean zero, or that is, $\overline{n^a} = 0$, where the overbar denotes an ensemble average. Then the covariance matrix of the noise \mathcal{C}^{ab} is defined as,

$$\mathcal{C}^{ab} = \overline{n^a n^b}. \quad (2.8)$$

If the noise is assumed to be stationary and ergodic then there exists a noise autocorrelation function $K(t)$ such that $\mathcal{C}^{ab} = K(|a - b|\Delta)$. In the Fourier basis it can be shown that the components of the noise vector are statistically independent [10] and the covariance matrix in the Fourier basis will contain only diagonal terms whose values will be strictly positive: $\tilde{\mathcal{C}}^{aa} = \overline{\tilde{n}^a \tilde{n}^{*a}}$. This implies that the covariance matrix has strictly positive eigenvalues. The diagonal elements of this matrix $\tilde{\mathcal{C}}^{aa}$ constitute the discrete representation of the power spectrum of the noise $S_n(f)$.

Gaussian noise can be described by the distribution,

$$p_0(\mathbf{n}) = M_n \exp \left[-\frac{1}{2} \sum_{a,b=0}^{N-1} [\mathcal{C}^{-1}]_{ab} n^a n^b \right], \quad (2.9)$$

where M_n is a normalization constant given by,

$$M_n = \left[(2\pi)^N \det [\mathcal{C}^{ab}] \right]^{-1/2}.$$

Equivalently in the Fourier domain this can be written as,

$$\begin{aligned} p_0(\mathbf{n}) &= M_n \exp \left[-\frac{1}{2} \sum_{a,b=0}^{N-1} [\tilde{\mathcal{C}}^{-1}]_{ab} \tilde{n}^a \tilde{n}^{b*} \right] \\ &= M_n \exp \left[-\frac{1}{2} \sum_{a=0}^{N-1} \tilde{n}^a \tilde{n}^{a*} / \tilde{\mathcal{C}}^{aa} \right], \end{aligned} \quad (2.10)$$

where in the last step we have used the diagonal property of the matrix $\tilde{\mathcal{C}}^{ab}$ which implies that $[\tilde{\mathcal{C}}^{-1}]_{aa} = 1/\tilde{\mathcal{C}}^{aa}$.

In the presence of the signal $\mathbf{s}(\check{\boldsymbol{\mu}})$ the above probability density function (pdf) gets modified but in a very simple way since we have assumed that the noise is additive. We have,

$$p_1(\mathbf{x}) = p_0(\mathbf{x} - \mathbf{s}(\check{\boldsymbol{\mu}})), \quad (2.11)$$

where $p_1(\mathbf{x})$ is the pdf of \mathbf{x} when the signal $\mathbf{s}(\check{\boldsymbol{\mu}})$ is present in the data stream.

In this paper we shall assume the noise to have a power spectrum consistent with the initial LIGO instrument. We use the fit to the noise curve as given in [16]:

$$S_n(f) = S_0 \left[\left(\frac{f}{200} \right)^{-4} + 2 \left(1 + \frac{f}{200} \right)^2 \right]. \quad (2.12)$$

The value of S_0 will not concern us since what matters is only the ratio of the signal amplitude to that of the noise, in other words the SNR. We shall set the value of S_0 to be unity and accordingly adjust the amplitude of the signal to get the required SNR.

C. The Matched Filter

In the absence of any prior information it must be assumed that all the parameter values, within their respective range, are equally likely to occur. In such a case, the method of maximum likelihood can be used. When the noise is a stationary Gaussian random process, the method of MLE reduces to the so called matched filtering technique. Matched filtering involves correlating the detector output with a bank of matched filters each of which corresponds to the signal waveform for a fixed set of parameters. To this end, we define a scalar product on \mathcal{V} . In the continuum limit the scalar product between two vectors \mathbf{x} and \mathbf{y} is given by,

$$\langle \mathbf{x}, \mathbf{y} \rangle = \int_0^\infty df \frac{1}{S_n(f)} (\tilde{x}(f) \tilde{y}^*(f) + \tilde{x}^*(f) \tilde{y}(f)) , \quad (2.13)$$

where, the Hermitian property of the Fourier transform of a real function has been used to restrict the domain of integration to positive frequencies. $S_n(f)$ is the power spectral density of the noise. The Fourier domain is convenient since stationarity of the noise has been assumed. The norm of a vector \mathbf{z} will be denoted by $\|\mathbf{z}\| = \langle \mathbf{z}, \mathbf{z} \rangle^{1/2}$. In eqn. (2.6) we had left \mathcal{N} undefined. We choose the value of \mathcal{N} such that $\|\mathbf{s}(\boldsymbol{\mu})\| = A$. From the definition of the scalar product in eqn. (2.13) and from eqn. (2.6) it follows that,

$$\frac{1}{\mathcal{N}^2} = 2 \int_0^{\infty} \frac{f^{-7/3}}{S_n(f)} df. \quad (2.14)$$

The integrand in the above equation, $I(f)$ is plotted in Fig. 1. This function peaks at around $f = 135\text{Hz}$ and a major contribution to the integral comes from a region around 135Hz.

We shall use normalized matched filters, that is, we set $\mathbf{h}(\mu^j) = \mathbf{s}(\boldsymbol{\mu})/A$. Henceforth we shall use the symbols a, b, \dots to indicate indices whose range of values includes 0 which as an index denotes the amplitude parameter, *i.e.* $\mu^0 = A$. Indices i, j, \dots will not include the amplitude parameter and will never take the value 0.

The output called the correlation $c(\mu^j)$ of the matched filter with parameters μ^j is then just the scalar product given by,

$$c(\mu^j) = \langle \mathbf{x}, \mathbf{h}(\mu^j) \rangle. \quad (2.15)$$

Given the data vector \mathbf{x} , the correlation is computed for the entire feasible range of parameters, continuously over the kinematic parameters t_s and Φ and for discrete values of the dynamical parameters τ_0 and τ_1 . The filters corresponding to the discrete values of τ_0 and τ_1 constitute the filter bank. The maximum of $c(\mu^j)$ is computed and compared with a pre-assigned threshold determined from the false alarm probability. A detection is announced if the maximum of $c(\mu^j)$ crosses the threshold. The parameters $\hat{\mu}^j$ for which the correlation is maximised are the MLE of the parameters of the signal. However, these will in general differ from the actual signal parameters $\check{\mu}^j$ due to the presence of noise. The difference $\Delta\mu^j = \check{\mu}^j - \hat{\mu}^j$ is the error made in estimating the parameters. When the signal is weak as compared to the noise (low SNR), the estimated parameters in general will differ by a large margin from the true ones, while in the limit of high SNR, the two will almost coincide. Thus in general $\Delta\mu^j$ is not small.

Let the data vector be

$$\mathbf{x} = \check{A}\mathbf{h}(\check{\mu}^j) + \mathbf{n}, \quad (2.16)$$

where \check{A} is the amplitude of the signal and $\check{\mu}^j$ are the remaining parameters. We have

separated the amplitude as it occurs in the signal as just a scale factor multiplying the signal. The SNR is defined as,

$$\rho = \langle \mathbf{s}(\check{\boldsymbol{\mu}}), \mathbf{s}(\check{\boldsymbol{\mu}}) \rangle^{1/2} = \check{A}. \quad (2.17)$$

From eqs. (2.6) and (2.13) we see that the SNR is equal to the amplitude parameter of the signal, \check{A} .

When we consider an ensemble of noise realisations, the $c(\mu^j)$ becomes a random variable. For a fixed set of parameters μ^j , $c(\mu^j)$ is a Gaussian random variable since it is a linear function of the noise (eqn. (2.15)). The process of maximization over the parameters is however a nonlinear process and hence the statistics of $c(\mu^j)$ will be non-Gaussian. For a given realization of noise, we assume that the global maximum of $c(\mu^j)$ will also be a local maximum. This assumption depends on the specific nature of the waveform and the filter bank. The equations which will be satisfied at the estimated parameters $\mu^j = \hat{\mu}^j$, are,

$$\begin{aligned} \frac{\partial c}{\partial \mu^i} &= 0 \\ \Rightarrow \left\langle \check{A} \mathbf{h}(\check{\mu}^j) + \mathbf{n}, \frac{\partial \mathbf{h}}{\partial \mu^i} \right\rangle &= 0 \\ \Rightarrow \left\langle \mathbf{h}(\check{\mu}^j), \frac{\partial \mathbf{h}}{\partial \mu^i} \right\rangle &= -\frac{1}{\check{A}} \left\langle \mathbf{n}, \frac{\partial \mathbf{h}}{\partial \mu^i} \right\rangle. \end{aligned} \quad (2.18)$$

In the limit of high SNR the mean square errors in the measurement of the parameters are characterised by the so called covariance matrix C^{ab} [10] defined as,

$$\Gamma_{ab} = \left\langle \frac{\partial \mathbf{s}}{\partial \mu^a}(\boldsymbol{\mu}), \frac{\partial \mathbf{s}}{\partial \mu^b}(\boldsymbol{\mu}) \right\rangle \quad (2.19)$$

$$C^{ab} = [\Gamma^{-1}]^{ab} \quad (2.20)$$

From the expression for the Fourier transform in the stationary phase approximation (eqn. (2.6)) and from the definition of the scalar product (eqn. (2.13)) we see that the phase function in the Fourier transform simply cancel out and only the amplitude remains. We also find that $C^{ab} \propto \check{A}^{-2}$.

The idea now is to compare the results of the Monte Carlo simulations with those obtained via eqn. (2.19). In the limit of high SNR, it is expected that the errors will agree with

those obtained from the covariance matrix. In the following sections we briefly mention the results of the Monte Carlo simulations and then analyse in detail eqn. (2.18). The goal is to first check the agreement between the two and then understand how the additional errors arise by studying the consequences of eqn. (2.18).

III. THE NEWTONIAN WAVEFORM

A. Monte Carlo Simulations

In this section we shall restrict ourselves to the Newtonian waveform. We have the four parameters:

$$\boldsymbol{\mu} \equiv \mu^a \equiv \{\mu^0, \mu^1, \mu^2, \mu^3\} \equiv \{A, 2\pi f_s t_s, \Phi, 2\pi f_s \tau_0\}.$$

Simulations were carried out for a test case of $\check{\tau}_0 = 5.558$ s This corresponds to a binary comprised of a $10M_\odot$ black hole and a $1.4M_\odot$ neutron star. The waveform was cutoff at a frequency of 800 Hz and the data train was sampled at 2000Hz. As mentioned before the power spectral density was chosen to be consistent with the initial LIGO interferometer. The range of τ_0 for the filters was $[5.358, 5.758]$ with a spacing of 1 msec. The simulations presented here were carried out for an SNR of 10, *i.e.*, $\check{A} = 10$. We considered 12000 realizations of noise.

The covariance matrix for the Newtonian case is given below:

$$\mathbf{C}_{(\boldsymbol{\mu})} \equiv [C_{(\boldsymbol{\mu})}^{ab}] = \frac{1}{\check{A}^2} \begin{pmatrix} \check{A}^2 & 0.0 & 0.0 & 0.0 \\ 0.0 & 222.50 & 322.26 & -227.25 \\ 0.0 & 322.26 & 469.16 & -328.65 \\ 0.0 & -227.25 & -328.65 & 232.26 \end{pmatrix} \quad (3.1)$$

In the above the diagonal values denote the variances in the parameters and the nondiagonal components denote the covariances between the parameters. Since the components do not depend on the parameters μ^j , (see [22,19] for details) we can choose a new set of parameters in which the covariance matrix is diagonal. The transformation can be affected by means of

an orthogonal transformation. We have the new parameter set $\boldsymbol{\nu} \equiv \{A, \nu^1, \nu^2, \nu^3\}$, related to $\boldsymbol{\mu}$ by means of the relation $\boldsymbol{\nu} = \mathbf{S}\boldsymbol{\mu}$, where \mathbf{S} is a orthogonal matrix, which for our particular case is:

$$\mathbf{S} = \begin{pmatrix} 1.0 & 0.0 & 0.0 & 0.0 \\ 0.0 & -0.794 & 0.129 & -0.594 \\ 0.0 & 0.359 & -0.690 & -0.629 \\ 0.0 & -0.491 & -0.713 & 0.501 \end{pmatrix} \quad (3.2)$$

In this new coordinate system the covariance matrix $\mathbf{C}_{(\nu)} = \mathbf{S}\mathbf{C}_{(\mu)}\mathbf{S}^{-1}$, and is given by,

$$\mathbf{C}_{(\nu)} = \frac{1}{\check{A}^2} \begin{pmatrix} \check{A}^2 & 0.0 & 0.0 & 0.0 \\ 0.0 & 0.024 & 0.0 & 0.0 \\ 0.0 & 0.0 & 1.640 & 0.0 \\ 0.0 & 0.0 & 0.0 & 922.3 \end{pmatrix} \quad (3.3)$$

In the high SNR limit the root mean square errors in the parameters ν^a are given by,

$$\sigma_{\nu^a} = \sqrt{C^{aa}}. \quad (3.4)$$

For an SNR of 10 the values are $\{1.0, 0.015, 0.128, 3.037\}$.

In a previous work [19] we had performed detailed Monte Carlo simulations to study the variation of the errors with the SNR. The simulations carried out in that paper were with a slightly different power spectrum, as we have used a simple fit to the noise curve in this paper. We reproduce in Fig. 2, the variation of errors in the parameters with the SNR as given in Figure 5 of [19] for the parameters τ_0 and t_a , except that we use the log scale for both the axis, as is conventional in statistical literature. The continuous line represents the errors computed via the covariance matrix and in this approximation the errors are inversely propotional to the SNR. The dotted line represents the errors as obtained from the Monte Carlo simulations. The rest of this paper tries to explain the discrepancy between the two curves in this figure at low SNRs $\rho \approx 10$.

B. The equation for the errors

The expression for the Fourier transform of the chirp in eqn. (2.6) in the new coordinates retains its form, but the functions $\chi_i(f)$ are now transformed to,

$$\eta_i(f) = \sum_{j=1}^3 \chi_j \left[S^{-1} \right]_i^j.$$

Rewriting eqn. (2.18) in the new parameters we have at $\nu^j = \hat{\nu}^j$,

$$\kappa_i = -\frac{1}{\tilde{A}} \left\langle \mathbf{n}, \frac{\partial \mathbf{h}}{\partial \nu^i} \right\rangle = \left\langle \mathbf{h}(\check{\nu}^j), \frac{\partial \mathbf{h}}{\partial \nu^i} \right\rangle. \quad (3.5)$$

Using the definition of the scalar product in eqn. (2.13), we have,

$$\kappa_i = 2\mathcal{N}^2 \int_0^\infty \frac{f^{7/3} \eta_i(f) \sin\left(\sum_{j=1}^3 \eta_j(f) \Delta \nu^j\right)}{S_n(f)} df, \quad (3.6)$$

where $\Delta \nu^j = \hat{\nu}^j - \check{\nu}^j$. In the Newtonian case these constitute a set of three nonlinear equations connecting ν^i to κ_i . The quantities κ_i are random variables. Since $\hat{\nu}^i$ depend upon \mathbf{n} , κ_i are in general nonlinear functions of the noise. This implies that the statistics of κ_i can in general be non-Gaussian. However, for chirp signals of the type we consider, the statistics of κ_1 and κ_2 will turn out to be Gaussian. This will be demonstrated in the next section. We define the total phase difference θ between the signal and the filter as,

$$\theta(f, \Delta \nu^i) = \sum_{j=1}^3 \eta_j(f) \Delta \nu^j, \quad (3.7)$$

which is relevant for future considerations. In the high SNR limit the errors $\Delta \nu^j$ are small and hence we can make the approximation $\sin(\theta) \simeq \theta$. This corresponds to using the covariance matrix to provide an estimate of the errors. At astrophysically interesting SNRs ≈ 10 this assumption does not hold.

It is clear that a good correlation between two waveforms is obtained when the phase difference between the two waveforms is a multiple of 2π and is roughly constant over the time for which the waveforms last. This assumption is found to be true in the simulations. Even though there are far more outlying points than what is predicted by the covariance

matrix the phase difference between the signal and the optimally matching template is found to be roughly constant. A typical case is illustrated in Fig. 3, in which θ is plotted as a function of frequency for $\Delta\nu^i \equiv \{1.62, -8.49, 7.3\}$. The function $\theta(f)$ is found to be close to -4π in the region around 135 Hz, from which the maximum contribution to the SNR is obtained. Note that the values of $\Delta\nu^1$ and $\Delta\nu^2$ are way beyond the rms errors predicted by the covariance matrix.

Since the function $I(f)$ in Fig. 1 peaks at $f \approx 135\text{Hz.}$, we define θ_m to be the value of θ at $f = 135\text{Hz.}$, *i.e.*,

$$\theta_m = -3.87615\Delta\nu^1 + 0.739347\Delta\nu^2 + -0.0149334\Delta\nu^3. \quad (3.8)$$

In Fig. 4 we illustrate how the θ_m is distributed across many realizations of noise. It is clear from the figure that θ_m is strongly clustered around multiples of 2π . Since θ_m is a linear combination of the parameters, it is clear that at least some of the parameters will show similar clustering properties. The variable θ_m is a very convenient indicator of the rough location of the parameters in the parameter space. If the absolute value of θ_m is large then the estimated parameters are far away from the actual value of the parameters.

Fig. 5 is a $\nu^1 - \nu^2$ scatter plot, where each point corresponds to a realization of noise. The plot shows that ν^1 and ν^2 parameters are clustered in well separated ‘islands’ in the parameter space considered. The variable θ_m computed for points in any specific island yield values close to a specific integral multiple of 2π depending upon the island we choose. Multiple solutions to eqn. (3.6) are responsible for the islands. Since the pdf in the κ_i space is largest at the origin, the islands correspond to $\theta(f) \simeq 2k\pi$, where k is an integer. We give an explanation of this below. The phase parameter $\mu^2 \equiv \Phi$ is constrained to lie in the interval $[-\pi, \pi]$. Using the relation $\mu^i = [S^{-1}]_j^i \nu^j$, we have,

$$\Phi \equiv \mu^2 = 0.129212\nu^1 + -0.689524\nu^2 + -0.712644\nu^3. \quad (3.9)$$

Since the rms error in ν^3 as calculated from the covariance matrix at an SNR of 10 is 3.04, it is highly likely that the absolute value of the last term in eqn. (3.9), (which dominates

the other terms in the same equation, since the rms errors for the other parameters are much lesser) exceeds π . This forces the parameters ν^1 and ν^2 to *jump* to values such that Φ remains in the range $[-\pi, \pi]$. In order to calculate the amount by which the parameters jump, we consider eqn. (3.8). Since θ_m must be a multiple of 2π in order to get a good match, each of the first two terms on the right hand side of eqn. (3.8) contributes π . This implies that ν^1 jumps by $\pi/3.87615 \approx .81$ and ν^2 jumps by $\pi/0.739347 \approx 4.25$. Since the two terms are of opposite signs, we find that ν^1 increases when ν^2 decreases and vice versa.

We now revert back to eqn. (3.6). Since θ is close to an integral multiple of 2π in the frequency region of interest, we can write,

$$\sin(\theta) \approx \left(\sum_{j=1}^3 \eta_j(f) \Delta \nu^j - 2k\pi \right), \quad (3.10)$$

for some integer k . We have,

$$\kappa_i = 2\mathcal{N}^2 \sum_{j=1}^3 \int_0^\infty \frac{f^{7/3} \eta_i(f) \eta_j(f) \Delta \nu^j}{S_n(f)} df - 4k\pi \mathcal{N}^2 \int_0^\infty \frac{f^{7/3} \eta_i(f)}{S_n(f)} df. \quad (3.11)$$

Since the ν coordinate system is orthogonal,

$$\int_0^\infty \frac{f^{7/3} \eta_i(f) \eta_j(f) \Delta \nu^j}{S_n(f)} df = 0 \quad \text{for } i \neq j, \quad (3.12)$$

and

$$2\mathcal{N}^2 \int_0^\infty \frac{f^{7/3} \eta_i(f)^2}{S_n(f)} df = \frac{1}{C_{(\nu)}^{ii}}. \quad (3.13)$$

Therefore,

$$\kappa_i = \frac{\Delta \nu^i}{C_{\nu}^{ii}} - 2k\pi G_i, \quad (3.14)$$

where,

$$G_i = 2\mathcal{N}^2 \int_0^\infty \frac{f^{7/3} \eta_i(f)}{S_n(f)} df. \quad (3.15)$$

The amount by which the parameters ν^1 and ν^2 jump can be calculated more accurately using eqn. (3.14). For two successive values of the integer k , the parameter ν^1 has to jump

by, $2\pi G_1/C_\nu^{11}$ in order to have the same value of κ_1 . This works out to be 0.812 for the parameter ν^1 . Similarly the value for the parameter ν^2 turns out to be 4.332. These values are consistent with the scatter plot in Fig. 5.

It is clear from Fig. 5 that the distribution of the parameters ν^1 and ν^2 will be markedly multimodal. However, the distribution of ν^3 is relatively smoother. This is illustrated in Fig. 6 which is a scatter plot on the $\nu^2 - \nu^3$ plane. Though there are gaps along the ν^2 axis, ν^3 takes all values in the range shown. The parameter ν_3 is relatively well behaved, *i.e.* it does not exhibit any sudden jumps like the other parameters.

The variances as obtained from the Monte Carlo simulations in the parameters ν^i are, $\Sigma_{\nu^i} \equiv \{0.421, 2.26, 2.53\}$ whereas, the values predicted by the covariance matrix are $\sigma_{\nu^i} \equiv \{0.0153, 0.1281, 3.037\}$. In the case of the parameters ν^1 and ν^2 the observed variances are much larger than the lower bounds, due to the jumps which these parameters make. However we notice that the observed variance in the case of ν^3 is actually *less* than the lower bound. This is due to the fact that the Cramer-Rao bounds are applicable only to parameters which are allowed to vary freely. For instance the variance for the parameter $\Phi \equiv \mu^2$ can have the maximum value of π^2 whatever be the SNR. The restriction of the range of μ^2 puts a constraint on the values of the parameters ν^j and this accounts for the observed error being less than the Cramer-Rao bound. In the next section we give a more quantitative model for the distribution of the parameters.

C. Geometrical Perspective

In this section we use differential geometry to arrive at a statistical model for the distribution of the parameters. The model described here is quite general and is applicable to the estimation of parameters obtained by means of the maximum likelihood method, for an arbitrary signal in the presence of Gaussian noise. The set of signal vectors, $\mathbf{s}(\boldsymbol{\nu}) \equiv s(t; \boldsymbol{\nu})$, where $\boldsymbol{\nu} \equiv \{\nu_0, \dots, \nu_{m-1}\}$, is a m -dimensional parameter vector, will describe a m -dimensional manifold \mathcal{S} embedded in \mathcal{V} , the vector space of all detector outputs. (See [19,24] for an

introduction to the use of differential geometry in gravitational wave data analysis, and [25] for the application of differential geometry to statistics.) Let the output of a detector \mathbf{x} , contain a signal $\mathbf{s}(\check{\boldsymbol{\nu}})$. Then $\mathbf{x} = \mathbf{s}(\check{\boldsymbol{\nu}}) + \mathbf{n}$, where \mathbf{n} is a noise vector drawn from the noise distribution. The distance, $D(\boldsymbol{\nu})$ between \mathbf{x} and a point $\mathbf{s}(\boldsymbol{\nu})$ is given by,

$$D(\boldsymbol{\nu}) = \|\mathbf{x} - \mathbf{s}(\boldsymbol{\nu})\| = \langle \mathbf{x} - \mathbf{s}(\boldsymbol{\nu}), \mathbf{x} - \mathbf{s}(\boldsymbol{\nu}) \rangle^{1/2}, \quad (3.16)$$

$$= [\langle \mathbf{x}, \mathbf{x} \rangle - 2 \langle \mathbf{x}, \mathbf{s}(\boldsymbol{\nu}) \rangle + \langle \mathbf{s}(\boldsymbol{\nu}), \mathbf{s}(\boldsymbol{\nu}) \rangle]^{1/2}. \quad (3.17)$$

The MLE of the parameters is that point $\hat{\boldsymbol{\nu}}$ on the parameter space which minimises $D(\boldsymbol{\nu})$. This is equivalent to maximising the correlation $c(\boldsymbol{\nu}) = \langle \mathbf{x}, \mathbf{s}(\boldsymbol{\nu}) \rangle$ provided we keep $\langle \mathbf{s}(\boldsymbol{\nu}), \mathbf{s}(\boldsymbol{\nu}) \rangle$ constant.

In the limit of high SNR, $\mathbf{s}(\hat{\boldsymbol{\nu}})$ will lie in a small region around $\mathbf{s}(\check{\boldsymbol{\nu}})$ on the manifold, effectively the tangent space to the manifold at $\mathbf{s}(\check{\boldsymbol{\nu}})$. In this case, the difference, $\mathbf{s}(\hat{\boldsymbol{\nu}}) - \mathbf{s}(\check{\boldsymbol{\nu}})$ can be satisfactorily approximated as the projection of the noise vector onto the tangent space. This implies that $\mathbf{s}(\hat{\boldsymbol{\nu}}) - \mathbf{s}(\check{\boldsymbol{\nu}})$ is linear function of \mathbf{n} . Further, if the parameters form a Cartesian system of coordinates, then, they too will be linear in \mathbf{n} and the distribution of the parameters can be described by a multivariate Gaussian [12]. The covariance matrix of this distribution defines a lower bound on the errors in estimation and is termed as the Cramer-Rao bound.

If the global minimum of $D(\boldsymbol{\nu})$ is also a local minimum then, at $\boldsymbol{\nu} = \hat{\boldsymbol{\nu}}$,

$$\partial D(\boldsymbol{\nu}) / \partial \nu^a = 0, \quad \text{for } a = 0, \dots, m-1 \quad (3.18)$$

which implies,

$$\left\langle \mathbf{s}(\check{\boldsymbol{\nu}}) + \mathbf{n} - \mathbf{s}(\hat{\boldsymbol{\nu}}), \frac{\partial \mathbf{s}}{\partial \nu^a}(\hat{\boldsymbol{\nu}}) \right\rangle = 0. \quad (3.19)$$

These are a set of m equations, one for each parameter. We interpret these equations geometrically as follows. The equations imply that the vector $\mathbf{x} - \mathbf{s}(\hat{\boldsymbol{\nu}})$ is orthogonal to each of the coordinate basis vectors, $\partial / \partial \nu^a$, evaluated at $\boldsymbol{\nu} = \hat{\boldsymbol{\nu}}$. Thus $\hat{\boldsymbol{\nu}}$ is a local extremum when the tip of the vector \mathbf{x} lies on that $N - m$ dimensional hyperplane $\mathcal{B}_{\hat{\boldsymbol{\nu}}}$, which passes through

$\mathbf{s}(\hat{\boldsymbol{\nu}})$, and is orthogonal to the m -dimensional tangent plane at $\mathbf{s}(\hat{\boldsymbol{\nu}})$. This hyperplane, $\mathcal{B}_{\hat{\boldsymbol{\nu}}}$, is the intersection of the $(N-1)$ -dimensional hyperplanes, $\mathcal{N}_{\hat{\boldsymbol{\nu}}}^a$, each orthogonal to a coordinate basis vector $\partial/\partial\nu^a$ at $\boldsymbol{\nu} = \hat{\boldsymbol{\nu}}$.

Let \mathbf{l}_a be the normalized coordinate basis vectors at $\hat{\boldsymbol{\nu}}$, *i.e.*

$$\mathbf{l}_a = \frac{\partial \mathbf{s}}{\partial \nu^a}(\hat{\boldsymbol{\nu}}) / \left\| \frac{\partial \mathbf{s}}{\partial \nu^a}(\hat{\boldsymbol{\nu}}) \right\|. \quad (3.20)$$

We define r_a to be the minimal distance from $\mathbf{s}(\check{\boldsymbol{\nu}})$ to the hyperplane $\mathcal{N}_{\hat{\boldsymbol{\nu}}}^a$, which is given by

$$r_a = \langle \mathbf{s}(\hat{\boldsymbol{\nu}}) - \mathbf{s}(\check{\boldsymbol{\nu}}), \mathbf{l}_a \rangle. \quad (3.21)$$

A schematic illustration of the above discussion is given in Fig. 7.

The pdf for the vector \mathbf{x} to lie on $\mathcal{N}_{\hat{\boldsymbol{\nu}}}^a$ can depend only on \mathbf{l}_a and r_a . If the vector \mathbf{x} is to lie on $\mathcal{B}_{\hat{\boldsymbol{\nu}}}$, then it must simultaneously lie on each of the normal hyperplanes, $\mathcal{N}_{\hat{\boldsymbol{\nu}}}^a$. The pdf for \mathbf{x} to lie on $\mathcal{B}_{\hat{\boldsymbol{\nu}}}$ is given by the expression,

$$p(r_a) = \int_{\mathcal{V}} \left[\prod_{a=0}^{m-1} \delta(\langle (\mathbf{n} - r_a \mathbf{l}_a), \mathbf{l}_a \rangle) \right] p(\mathbf{n}) d^N n, \quad (3.22)$$

where the δ denotes the Dirac Delta function. Substituting for the Gaussian distribution for the noise $p(\mathbf{n})$ in the equation above and integrating, we get,

$$p(r_0, r_2, \dots, r_{m-1}) = \frac{\exp \left[-\frac{1}{2} \sum_{a,b=0}^{m-1} [\gamma^{-1}]^{ab} r_a r_b \right]}{[(2\pi)^m \det [\gamma_{ab}]]^{1/2}}, \quad (3.23)$$

where, $\gamma_{ab} = \langle \mathbf{l}_a, \mathbf{l}_b \rangle$. The integration though tedious, is quite straightforward. Note that each of the Gaussian random variables r_a will have unit variance as is obvious from the definition of γ_{ab} . Moreover, the matrix γ_{ab} is very closely related to the Fisher information matrix Γ_{ab} as defined in eqn. (2.19). Whereas the components of the Fisher information are got by taking scalar products of the tangent vectors on the manifold, the components of the matrix γ_{ab} are obtained by taking scalar products of the *normalized* tangent vectors on the manifold.

D. Statistical model for the Newtonian Chirp

We now specialise to the case of the Newtonian chirp. We use the parameters ν^a defined earlier, in the previous section. Since $\mathbf{s}(\hat{\nu}) = \hat{A}\mathbf{h}(\hat{\nu}^j)$, the above equations for \mathbf{l}_a and r_a give,

$$\mathbf{l}_0 = \mathbf{h}(\hat{\nu}^j), \quad (3.24)$$

$$\mathbf{l}_k = \frac{\partial \mathbf{h}}{\partial \nu^k}(\hat{\nu}^j) / \left\| \frac{\partial \mathbf{h}}{\partial \nu^k}(\hat{\nu}^j) \right\|, \quad (3.25)$$

$$r_0(\hat{\nu}^k, \hat{A}) = \check{A} \langle \mathbf{h}(\hat{\nu}^k), \mathbf{h}(\hat{\nu}^k) \rangle - \hat{A}, \quad (3.26)$$

$$r_j(\hat{\nu}^k) = \check{A} \left\langle \mathbf{h}(\hat{\nu}^k), \frac{\partial \mathbf{h}}{\partial \nu^j}(\hat{\nu}^k) \right\rangle / \left\| \frac{\partial \mathbf{h}}{\partial \nu^j}(\hat{\nu}^k) \right\|. \quad (3.27)$$

Since the ν coordinate system is orthogonal, γ_{ab} turns out to be nothing but the identity matrix. The distribution of the variables r_a is thus a joint Gaussian given by the expression,

$$p(r_0, \dots, r_3) = \frac{1}{2\pi^2} \exp \left[-\frac{1}{2} \sum_{a=0}^3 r_a^2 \right]. \quad (3.28)$$

The r_j variables are closely related to the κ_i variables defined in section III B in eqn. (3.5):

$$r_i = \check{A} \left\| \frac{\partial \mathbf{h}}{\partial \nu^i}(\hat{\nu}^k) \right\|^{-1} \kappa_i = \frac{\kappa_i}{\sqrt{\Gamma_{ii}}},$$

where we have used the definition of Γ_{ab} in eqn. (2.19). Thus they differ only by a factor which is simply a constant from eqs. (2.13) and (2.6). This is a consequence of the intrinsic flatness of the manifold [19] and the particular parameterization adopted.

From eqn. (3.28) we would expect the marginal probability distribution of each of the variables r_j to be a Gaussian distribution with unit variance. Using the ensemble of estimated parameters from the Monte Carlo simulations we can obtain the histograms and consequently the distributions of the variables r_j . In Fig. 8 we plot the probability distributions of the variables r_j , and compare them with the expected Gaussian distributions. It is clear that though r_1 and r_2 are Gaussian random variables to a good approximation, r_3 shows a pronounced non-Gaussian behaviour. The reason for this discrepancy can be traced to the fact that the phase parameter is constrained to lie in the range $[-\pi, \pi]$. In Fig. 6 we observe that in the central island the ν^3 parameter gets abruptly cutoff at a value of about

4.5 and -4.5 . Since the points on the central island are ‘close’ to the point corresponding to the actual value of the parameters, we can apply the eqn. (3.14) with $k = 0$. This gives a value of $\kappa_3 \approx 0.00488$ and consequently $r_3 \approx 1.5$. We observe in Fig. 8 that the dip in the distribution of r_3 occurs at the same point *i.e.* at $r_3 \approx 1.5$. To further elaborate on this point, we plot in the Fig. 9, the three variables r_i v/s the variable θ_m defined earlier. The figure clearly illustrates that while r_1 and r_2 take on their entire range of values in the central island, r_3 does not. This establishes a connection between the dip in the marginal distribution and the phase parameter being constrained to the range $[-\pi, \pi]$. Although a deeper understanding of this is in order, we continue our analysis assuming the distribution of r_3 to be given by a Gaussian.

Had the map between $\hat{\nu}$ to \mathbf{r} been bijective, it would have been possible to write the distribution for the estimated parameters simply as a product of the pdf for the variables r_a and a Jacobian factor. However, a given set of values for $\mathbf{r} \equiv \{r_a\}$ would in general correspond to multiple parameter vectors $\hat{\nu}^{(l)}$, where the range of values of l depends on the number of solutions. This is clear from Fig. 9 where we observe that the same value of r_j occurs for different values of the variable θ_m , and hence in different ‘islands’. We also observe that r_3 takes almost all its possible values in the central island and the two adjoining ones. Moreover, we notice that it is approximately true that r_3 takes different values in each of the three islands. Thus if we restrict ourselves only to the central and two adjoining islands, then the map between ν^j and r_j is bijective to a good degree of approximation. For a fixed set of values for $\{r_j\}$ we have therefore, a unique solution ν^j satisfying eqs. (3.27), if we restrict ourselves to the three islands identified above. We shall henceforth term the islands identified above as the *primary group* of islands and the solution there will be called the *primary* solution. (It is to be emphasized that the above discussion is applicable only to the Newtonian waveform. As we shall see later for the post-Newtonian case, the primary group of islands contains more islands on either side of the central island.) There will of course be other solutions in the other islands. It is to be noted that number of multiple solutions for a given set of values for $\{r_j\}$, depends on $\{r_j\}$, and we do *not* imply that each island

admits a solution ν^j for a fixed set of values for $\{r_j\}$. The reason for the term *primary* solution is to be found in Fig. 10, where we have plotted a histogram of the variable θ_m which gives us an idea as to how many points occur in each island. We observe that 99% of the points lie in the central and the two adjoining islands for the Newtonian case. Thus there is an overwhelming probability for the points to lie in one of these islands, and the primary solutions occur much more frequently as compared to the other solutions for a fixed value of r_j .

The problem now is to determine the various solutions $\hat{\nu}^{(l)}$ for a fixed set of values of $\{r_a\}$, and compute the probability that a particular $\hat{\nu}^{(m)}$ will be selected amongst others for a given \mathbf{r} . This is essentially the probability that the amplitude $\hat{A}^{(m)}$ is greater than the amplitude at the other solutions. We shall denote this probability as $P(\hat{\nu}^{(m)}|\mathbf{r})$. For a fixed set of values of $\{r_j\}$, we will have multiple solutions, $\{\hat{\nu}^j\}^{(1)}, \{\hat{\nu}^j\}^{(2)}, \dots$ to eqn. (3.27). The correlation obtained at these points will be

$$\hat{A}^{(l)} = \langle \mathbf{x}, \mathbf{h}(\hat{\nu}^j)^{(l)} \rangle.$$

It is to be noted that for a *fixed* $\{\hat{\nu}^j\}$, \hat{A} will be a Gaussian random variable with a variance of unity. In order to calculate $P(\{\hat{\nu}^j\}^{(l)}|\{r_j\})$ we need to identify all the solutions corresponding to a fixed set of values r_a . The identification of the multiple roots is quite a problem, and so we make the following approximation. We assume that for one of the solutions, that is the primary solution which we shall denote by $\{\hat{\nu}^j\}^{(1)}$, corresponding to $\{r_j\}$, the probability $P(\{\hat{\nu}^j\}^{(1)}|\{r_j\})$ is almost unity. If this is true, then, we only need to compute the probability that the correlation at an arbitrary point on the parameter space exceeds the correlation at the primary solution point which shares the same set of values of $\{r_j\}$. This corresponds to computing the probability of the Gaussian random variable $\hat{A}^{(l)}$, exceeding $\hat{A}^{(1)}$. Of course, $P(\{\hat{\nu}^j\}^{(1)}|\{r_j\})$ is set to unity. The justification for the above procedure is essentially the fact that nearly 99% of the points lie in the primary group of islands.

So for evaluating the distribution of the estimated parameters at $\nu^k = \hat{\nu}^k$ we follow the following procedure:

1. Determine $r_j(\hat{\nu}^k)$ using eqn. (3.27).
2. Determine $\{\hat{\nu}^k\}^{(1)}$ using eqn. (3.14) for an appropriate value of k , *i.e.* k takes one of the values $\{-1, 0, 1\}$.
3. Determine the probability for $\hat{A} = \langle \mathbf{x}, \mathbf{h}(\hat{\nu}^k) \rangle$ to be greater than $\hat{A}^{(l)} = \langle \mathbf{x}, \mathbf{h}(\hat{\nu}^k)^{(1)} \rangle$. (If $\hat{\nu}^k$ is already a primary solution then this probability is set to unity.)
4. Set $P(\{\nu^a\}|\{r_a\})$ equal to the calculated probability.
5. Write the the pdf of the estimated parameters as

$$p(\hat{\nu}) = \frac{1}{(2\pi)^2} J(\hat{\nu}) P(\hat{\nu}|\mathbf{r}) \exp \left[-\frac{1}{2} \sum_{a=0}^3 r_a^2(\hat{\nu}) \right], \quad (3.29)$$

where, $J(\hat{\nu})$ is the Jacobian of the transformation from $\hat{\nu}^a$ to the variables r_a , which is essentially,

$$J(\hat{\nu}) = \det \left[\frac{\partial r_a}{\partial \nu^b}(\hat{\nu}) \right]. \quad (3.30)$$

Since the amplitude parameter is not of primary interest to us, we shall integrate the distribution over \hat{A} . We use a threshold of 7, which means that we reject any realization whose measured value \hat{A} is less than 7 in the simulations. The amplitude parameter enters only via r_0 . So the distribution for the remaining three parameters $\hat{\nu}^k$ is,

$$p(\hat{\nu}^k) = \frac{1}{(2\pi)^{3/2}} J(\hat{\nu}^k) P(\hat{\nu}^k|\mathbf{r}) \exp \left[-\frac{1}{2} \sum_{i=1}^3 r_i^2(\hat{\nu}^k) \right] \times \frac{1}{(2\pi)^{1/2}} \int_{7.0}^{\infty} \exp \left[-\frac{1}{2} \left(\hat{A} \langle h(\hat{\nu}^k), h(\hat{\nu}^k) \rangle - \hat{A} \right)^2 \right] d\hat{A}. \quad (3.31)$$

Since the SNR is chosen to be 10 the second factor in the equation above is very close to unity.

We now compare the Monte Carlo results with the distribution given in eqn. (3.31). We compare the one dimensional marginal distribution $p(\hat{\nu}^1)$ with the histogram obtained via the Monte Carlo method. The marginal distribution $p(\hat{\nu}^1)$ is obtained by integrating eqn. (3.31)

with respect to ν^2 and ν^3 . This is done numerically. Though the parameter ν^1 has the least root mean square error of .015 as predicted by the covariance matrix, its distribution has the most pronounced non-Gaussian behaviour. In plot (a) and (b) of Fig. 11 we display the distributions $p(\hat{\nu}^1)$, obtained from the Monte Carlo simulations and the statistical model respectively. Plots (c) and (d) in the same figure zoom in on the first two maxima occurring on the right of the central maximum. It can be seen that in the case of plot (d) the match is not very good even though the location of the peaks match fairly well. The difference here could come from either the Monte Carlo method or the statistical model.

In the histogram of the variable θ_m illustrated in Fig. 10 we have seen that about 79.5% of the points in the simulations fall in the central island and about 10% in each of the adjoining islands at an SNR of 10. We can obtain the corresponding numbers from our theoretical model as given in eqn. (3.29), by integrating the distribution over all the parameters in the domain corresponding to each island. We obtain the values 82% for the central island and about 9.5% for each of the adjoining islands. Thus the statistical model shows good agreement with the Monte Carlo results by this criterion. The number of points in the subsequent islands falls off rapidly. The contribution to the variance from each island depends on the number of points in that region and the location of island in the parameter space. It is found that the maximum contribution to the variance comes from the islands immediately adjoining the central island.

IV. POST NEWTONIAN WAVEFORM

In the post-Newtonian case we have the five parameters,

$$\boldsymbol{\mu} \equiv \mu^a \equiv \{\mu^0, \mu^1, \mu^2, \mu^3\} \equiv \{A, 2\pi f_s t_s, \Phi, 2\pi f_s \tau_0, 2\pi f_s \tau_1\}.$$

Simulations (12000 realizations) were carried out again for an SNR of 10. The signal parameters were $\tilde{\tau}_0 = 5.558\text{s}$ and $\tilde{\tau}_1 = 0.684\text{s}$, corresponding to a binary comprised of a $10M_\odot$ black hole and a $1.4M_\odot$ neutron star. The simulation box taken was $\{5.058\text{s} \leq \tau_0 \leq$

$5.859\text{s}, 0.484\text{s} \leq \tau_1 \leq 0.985\text{s}$ }, with filter spacings of 10ms. in τ_0 and 5ms. in τ_1 . Our analysis of the post-Newtonian case will be very similar to the Newtonian case in section III. All the variables defined there can be defined for the post-Newtonian case also and we will use the same names for the variables to avoid using more symbols.

Here again we diagonalise the covariance matrix by making a coordinate transformation from the $\boldsymbol{\mu}$ to the $\boldsymbol{\nu}$ coordinate system. The diagonal covariance matrix in the $\boldsymbol{\nu}$ parameters is given by,

$$[C_{(\nu)}^{ab}] = \frac{1}{\tilde{A}^2} \begin{pmatrix} \tilde{A}^2 & 0.0 & 0.0 & 0.0 & 0.0 \\ 0.0 & 0.018 & 0.0 & 0.0 & 0.0 \\ 0.0 & 0.0 & 1.1974 & 0.0 & 0.0 \\ 0.0 & 0.0 & 0.0 & 403.64 & 0.0 \\ 0.0 & 0.0 & 0.0 & 0.0 & 15601.0 \end{pmatrix}$$

Therefore the root mean square errors in the parameters computed from the covariance matrix are, $\sigma_{\nu^i} \equiv \{.013, 0.109, 2.009, 12.49\}$. On the other hand the observed errors from the Monte Carlo simulations are $\Sigma_{\nu^i} \equiv \{1.33574, 7.43948, 5.34089, 23.049\}$. One finds as compared to the Newtonian case, the factors $\Sigma_{\nu^i}/\sigma_{\nu^i}$ are larger on the average. The reason for this is that here we have one more parameter, which means there are more filters which can match with the data and consequently there are more outlying points. This is evident from Fig. 12 as is explained below.

In Figs. 13 and 14 we give the scatter plots of the four parameters ν^i , the former on the $\nu^1 - \nu^2$ plane and the latter on the $\nu^3 - \nu^4$ plane. We observe that while there are gaps in distribution of the parameters ν^1 and ν^2 there are none in the distribution of the parameters ν^3 and ν^4 . Here the phase parameter $\mu^2 \equiv \Phi$ is given by,

$$\Phi = -0.109838\nu^1 - 0.621516\nu^2 + 0.695335\nu^3 + 0.343747\nu^4,$$

and the variable θ_m is given by,

$$\theta_m = 4.18241\Delta\nu^1 + 0.892242\Delta\nu^2 + 0.0186845\Delta\nu^3 + 0.00272864\Delta\nu^4.$$

Since both σ_{ν^3} and σ_{ν^4} are comparable, both these parameters will contribute to Φ as opposed to the Newtonian case where only the ν^3 parameter dominates. Thus we find that both the parameters ν^3 and ν^4 assume all their values in their respective ranges. The spacing between the islands in the ν^1 and ν^2 scatter plot is calculated to be $2\pi G_1/C_\nu^{11} = 0.69$ and $2\pi G_2/C_\nu^{22} = 3.90$ respectively. This is consistent with Fig. 13. In Fig. 13 we notice that there are more islands to the right than there are to the left of the central island. This is caused by the simulation box which is asymmetrical, *i.e.* the parameters of the signal are not at the center of the simulation box. This is so since all combinations of τ_0 and τ_1 do not correspond to valid masses for the components of the binary. This leads to a shift in the mean of the estimated parameters from their actual values. The observed means in the $\Delta\nu^i$ are $\{0.10167, 0.574784, -0.282783, 1.56494\}$. For higher SNRs the estimated parameters will tend to lie only on the islands which lie close to the central island and consequently within a symmetrical region around the actual values of the parameters. Therefore the bias will disappear for the case of higher SNRs.

In Fig. 12 we plot the histogram of the distribution of the variable θ_m in the post Newtonian case. Here, for the same SNR of 10, there are more outlying points as compared to the Newtonian case. This is to be expected since we have an additional parameter, and there is an additional degree of freedom to find the filter which matches best with the signal. The variance now gets substantial contributions even from far away islands as opposed to the Newtonian case.

In Fig. 15 we plot the variables r_i v/s θ_m . Here again only r_4 does not attain all its possible values within the central island, but now r_4 attains its entire range of values only when we include two islands on either side. Moreover the overlap of values of r_4 in these islands is much more pronounced as opposed to the Newtonian case and further investigations are needed to identify the primary solution correctly.

In Fig. 16 we plot the probability distributions of the variables r_i . The histograms are plotted using the Monte Carlo data and the continuous curve is a Gaussian with a variance of unity. It is clear that r_i are Gaussian random variables to a good degree of

approximation. The approximation is better than in the Newtonian case (see Fig. 8). As in the Newtonian case the r_i and κ_i are related by only a constant factor. Therefore κ_i are also Gaussian random variables. However, we note that this is true only for a special class of waveforms to which the chirp belongs. The chirp signal manifold is intrinsically flat and the parameterization of the waveform is such that the coordinates are essentially Cartesian. If some other parameterization is chosen (*e.g.* the chirp mass \mathcal{M}), the coordinates will no longer be so and κ_i will not be Gaussian random variables even though the variables r_i will remain Gaussian.

We can again as in the Newtonian case, write down the expression for the pdf of the estimated parameters. We do not write it explicitly here since the expression is formally the same as in eqn. (3.29), except now the index a runs from 0 to 4. We therefore only refer to eqn. (3.29) for the required pdf.

V. CONCLUSIONS

In this paper we have addressed the question of wide discrepancies between the theoretically predicted lower bounds in the errors in the estimation of parameters and the errors observed in numerical experiments. We now summarize in this section, the main results of our paper and indicate future directions.

- We find that the problem is of a *global* nature, in that the estimated values for the parameters fall into *disjoint* islands. Though there are very few points in the islands which are far from the actual value of the parameters, they contribute substantially to the variance. Thus the discrepancy between the Monte Carlo simulations and the Cramer Rao bounds cannot be resolved by using perturbative analysis. The restriction of the parameter Φ to the range $[-\pi, \pi]$ plays a major role in the non local distribution of parameters, as explained in the text.
- The problem is more transparent when we reparameterize the chirp signal so that the covariance matrix is diagonal in the new parameters. The parameters ν correspond to

choosing orthogonal coordinates on the chirp manifold. Since the covariances are zero for the variables r_a the pdf is computationally simpler to handle.

- A statistical model has been given which matches well with the distribution obtained from Monte Carlo simulations. The model is derived from geometrical considerations. We have identified certain variables r_i as Gaussian random variables and these play an important role in writing down the expression for the distribution of the estimated parameters.
- Since the distribution of the estimated parameters is multimodal, the variance is not a good indicator of the performance of the MLE. A more reasonable indicator would be to judge the performance of the MLE by means of confidence intervals *i.e.* compute the probability that the estimated parameters lie within a certain region around the actual value. As a concrete example, we compute the probability that the deviation of the estimated parameter is less than thrice the root mean square error at that SNR as predicted by the covariance matrix. We will use the symbol $P_{3\sigma}$ to denote the fraction of points which lie within the 3σ range for a given parameter. However this criterion will in general be dependent on the specific parameter chosen. Since τ_0 is one such physical parameter we use this to compute $P_{3\sigma}$.

In Figures 17 and 18 we plot $P_{3\sigma}$ v/s SNR for the parameter τ_0 in the Newtonian and the post-Newtonian cases respectively. The values of $P_{3\sigma}$ for the parameters such as τ_0 and τ_1 will be independent of the actual value of the chirp times. For this purpose we use the results of simulations carried out earlier in [19]. It is to be noted that whereas the simulations carried out in this paper use a single curve to fit the noise power spectrum, $S_n(f)$, we had used a more accurate representation of $S_n(f)$ in our earlier simulations [19]. We see that the MLE works moderately well even at low SNRs of $\rho \approx 10$. It is to be remarked that the assessment of an estimator depends upon how we use the estimates to calculate astrophysically interesting quantities.

- We required about 2 days of computation on a 300 MFlops (peak rating) machine to generate the results of this paper. The use of an integration routine specifically suited to the integrand, and/or the use of lookup tables for computing the integrand, would further speed up the computation substantially. The intrinsic flatness of the manifold turns out to be very convenient for our purpose. This property holds true for the first post-Newtonian waveform as well. There is one more parameter in the post-Newtonian waveform and consequently one more integration to perform to get the the marginal distribution of the parameters. For higher post-Newtonian corrections and/or for inclusion of parameters such as spins, it might be computationally expensive to compute the marginal distributions. However, it is to be noted that performing Monte Carlo simulations in such cases would also call for a huge amount of computational effort. A further research into the above issues is in progress.

ACKNOWLEDGMENTS

R.B. would like to thank CSIR, India for the senior research fellowship. S.D. would like to thank Bernard Schutz and Andrzej Krolak for fruitful discussions.

REFERENCES

- [1] A. Abramovici *et. al.*, Science, **256**, 325, (1992).
- [2] C. Bradaschia *et. al.*, Nucl. Instrum. Methods Phys. Res., Sect A 518 (1990).
- [3] B.F. Schutz, in *Gravitational Collapse and Relativity*, Edited by H. Sato and T. Nakamura, (World Scientific, Singapore, 1986), pp. 350-368.
- [4] D. Marković, Phys. Rev. D., **48**, 4738 (1993).
- [5] S. Finn, Phys.Rev. D., **53**, 2878, (1996).
- [6] L. Blanchet and B.S. Sathyaprakash, Phys. Rev. Lett., **74**, 1067 (1995).
- [7] K.S. Thorne, *Gravitational waves from compact objects*, to be published in *Proceedings of IAU symposium 165, Compact stars in binaries*, edited by J. van Paradijs, E. van den Heuvel, and E. Kuulkers, (Kluwer Academic Publishers).
- [8] K.S. Thorne, *Gravitational waves*, to be published in *Proceedings of the Snowmass 95 Summer Study on Particle and Nuclear Astrophysics and Cosmology*, edited by E.W. Kolb and R. Peccei, (World Scientific, Singapore).
- [9] K.S. Thorne, in *300 Years of Gravitation*, S.W. Hawking and W.Israel (eds.), (Cambridge Univ. Press, 1987).
- [10] C.W. Helstrom, *Statistical Theory of Signal Detection*, 2nd. ed, (Pergamon Press, London, 1968).
- [11] B.F. Schutz, in *The Detection of Gravitational Radiation*, edited by D. Blair (Cambridge, 1989) pp 406-427.
- [12] L. S. Finn, Phys. Rev. D **46**, 5236 (1992).
- [13] L.S. Finn and D.F. Chernoff, Phys. Rev. D **47**, 2198 (1993).
- [14] L. Blanchet and B.S. Sathyaprakash, Class. Quantum Grav., **11**, 2807 (1994).

- [15] A. Krolak, in *Gravitational wave data analysis*, edited by B.F. Schutz, (Dordrecht : Kluwer, 1989), pp. 59-69.
- [16] C. Cutler and E. Flanagan, *Phys.Rev. D* **49**, 2658 (1994).
- [17] A. Krolak, J. A. Lobo and B. J. Meers, *Phys. Rev D* **48**, 3451 (1993).
- [18] E. Poisson and C.M. Will, *Phys. Rev. D* **52**, 848 (1995).
- [19] R. Balasubramanian, B.S. Sathyaprakash and S.V. Dhurandhar, *Phys. Rev. D.*, **53**, 3033, (1996).
- [20] D. Nicholson and A. Vecchio, *Bayesian bounds on parameter estimation accuracy for coalescing binary gravitational wave signals*, gr-qc9705064.
- [21] C. Cutler *et al*, *Phys. Rev. Lett.* **70**, 2984 (1993).
- [22] B.S. Sathyaprakash, *Phys. Rev. D* **50**, R7111 (1994).
- [23] B.S. Sathyaprakash and S.V. Dhurandhar, *Phys. Rev. D* **44**, 3819 (1991).
- [24] B. J. Owen, *Phys. Rev. D*, **53**, 6749, (1996).
- [25] Shun-ichi Amari, *Differential Geometric Methods in Statistics* , (Springer-Verlag), (1987).

FIGURES

FIG. 1. Plot of $I(f)$ v/s f .

FIG. 2. Variation of root mean square errors in the parameters of the Newtonian waveform with SNR.

FIG. 3. Plot of θ_m v/s f ; $\Delta\nu^i \equiv \{1.62, -8.49, 7.3\}$. θ_m has a value close to -4π in the region around 135Hz, where $I(f)$ attains its maximum.

FIG. 4. Scatter plot of θ_m ; 12000 realizations of noise have been considered.

FIG. 5. Scatter plot on the $\nu^1 - \nu^2$ plane

FIG. 6. Scatter plot on the $\nu^2 - \nu^3$ plane

FIG. 7. Schematic illustration of the geometric picture discussed in the text.

FIG. 8. Marginal Probability distributions of the variables r^i .

FIG. 9. Plot of the variables r^i v/s θ_m .

FIG. 10. Histogram of the variable θ_m .

FIG. 11. Comparison between the statistical model and the Monte Carlo methods to arrive at the marginal distribution of the parameter ν^1 . Part (c) and (d) zoom in to the first and second maxima to the right of the central maximum.

FIG. 12. Histogram of θ_m for the post-Newtonian case.

FIG. 13. Scatter Plot on the $\nu^1 - \nu^2$ plane.

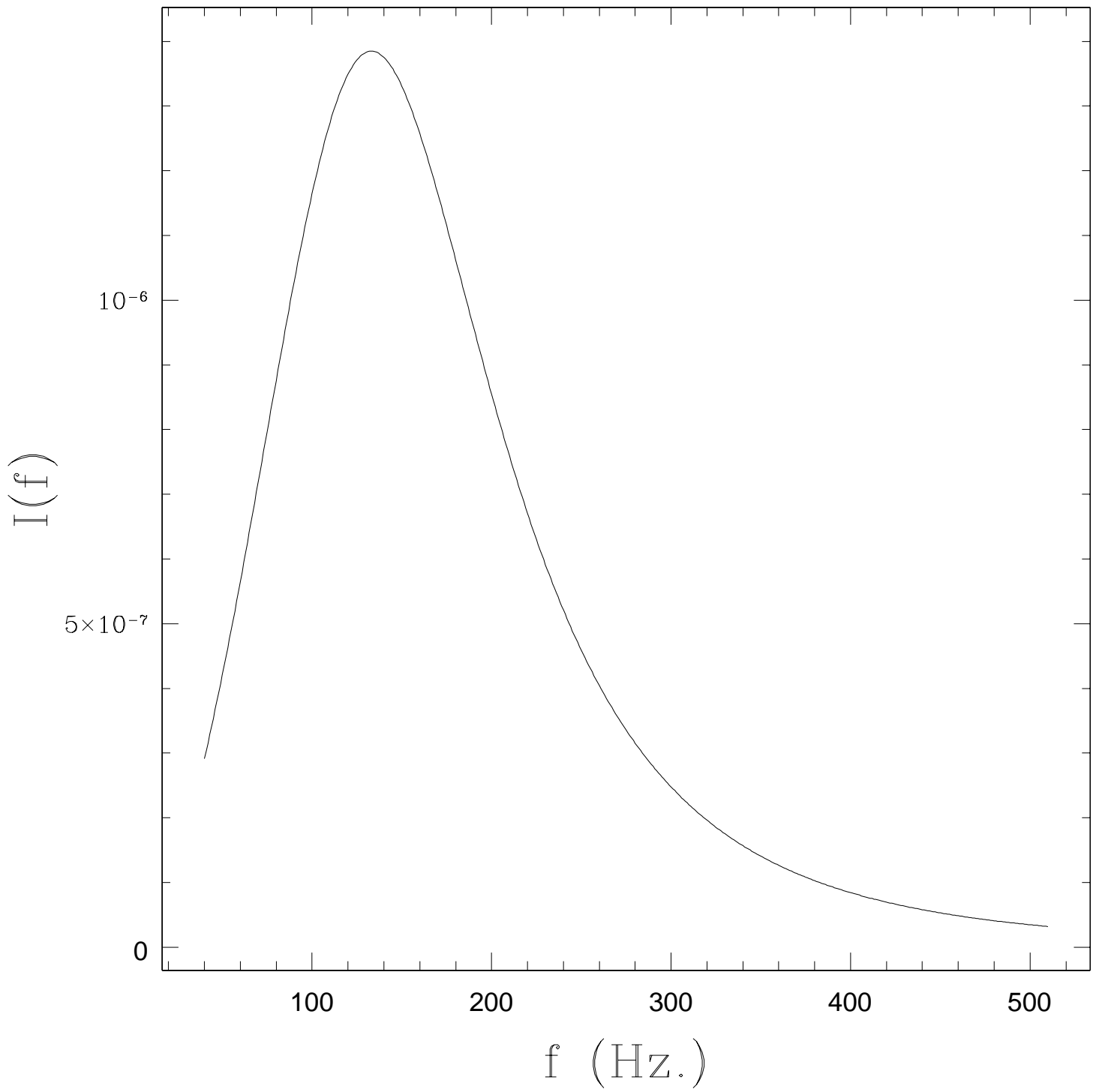
FIG. 14. Scatter Plot on the $\nu^3 - \nu^4$ plane.

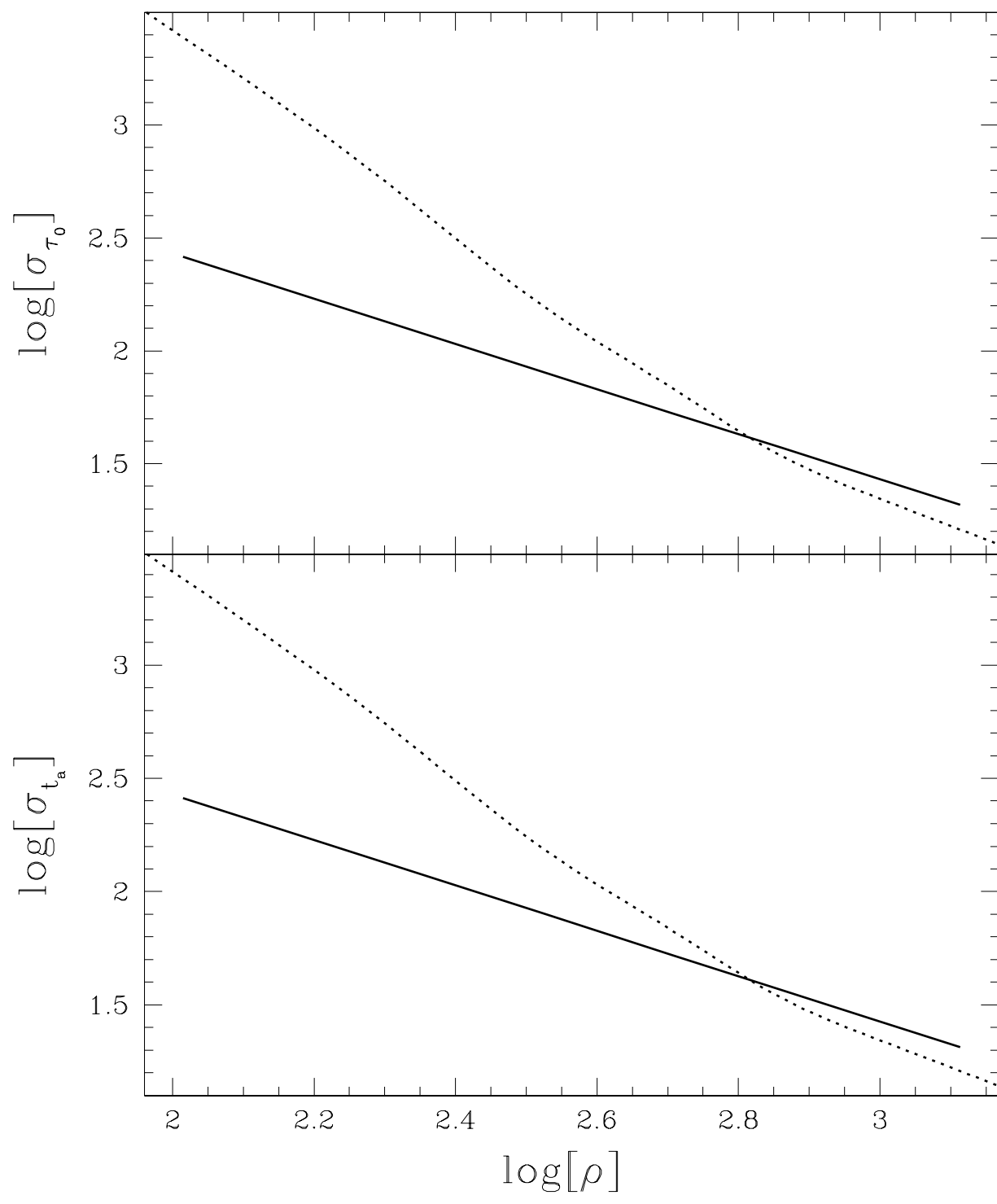
FIG. 15. Plot of the variables r^i v/s θ_m .

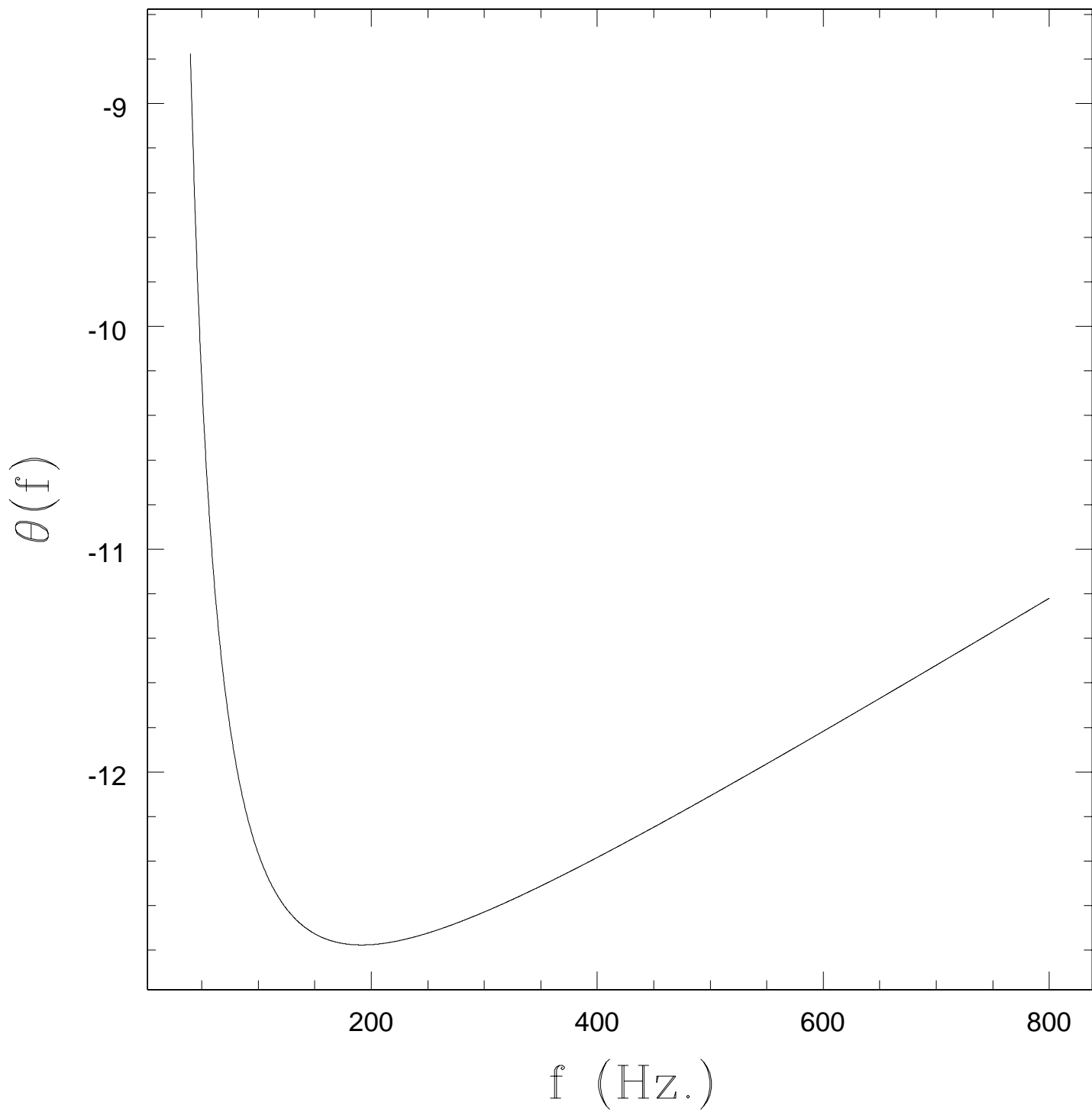
FIG. 16. Distributions of the variables r^i for the post-Newtonian case are plotted. The histogram is obtained from the Monte-Carlo simulations whereas the continuous curve is a unit variance Gaussian curve.

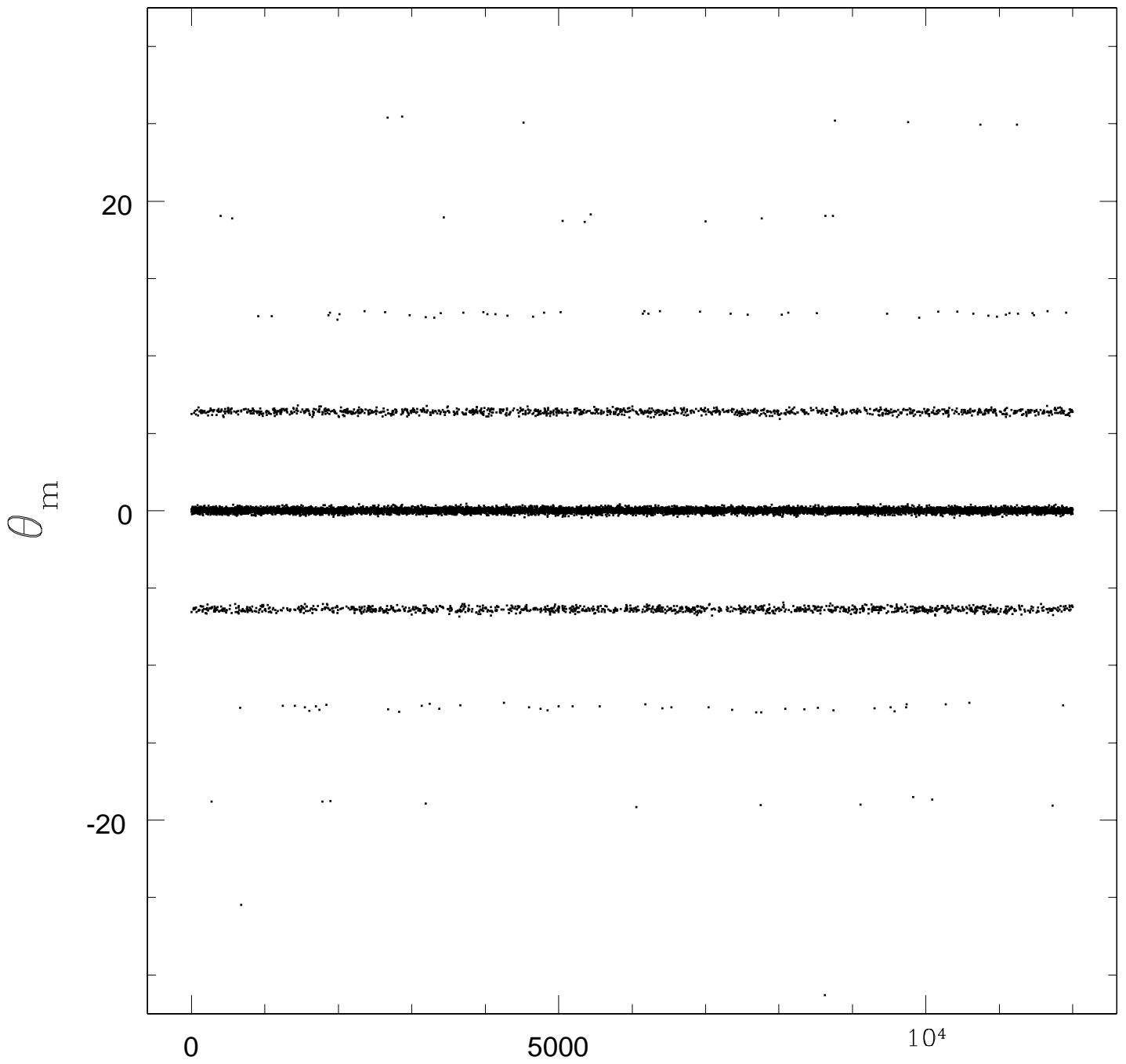
FIG. 17. Plot of $P_{3\sigma}$ for the parameter τ_0 v/s SNR for the Newtonian case.

FIG. 18. Plot of $P_{3\sigma}$ for the parameter τ_0 v/s SNR for the post-Newtonian case.









Noise Realizations

